From Small Crack Growth to Fatigue Life

E. Amsterdam[1], J.W.E. Wiegman[1], M. Nawijn[2]
[1]Royal Netherlands Aerospace Centre (NLR), Voorsterweg 31, Marknesse
[2]Colosso, Westeinde 5, Uffelte
THE NETHERLANDS

emiel.amsterdam@nlr.nl

Keywords: Physics of failure, total life approach, high cycle fatigue, stress life, short crack

ABSTRACT

The fatigue crack growth rate (FCGR) curve of metallic alloys is usually divided into three regions with steep slopes in regions I and III and a moderate linear slope in region II, which is often referred to as the Paris regime. However, there are many examples in literature that show that changes in the slope of region II are present. Linear behavior for regions I and III has been assumed by several researchers and led to a multi-linear description of the entire FCGR curve. In this paper we will assume that fatigue crack growth is governed by power law behavior at all crack lengths and all stress intensity factor ranges (ΔK). To accommodate for changes in the multi-linear FCGR curve, mathematical pivot points are introduced in the FCGR equation, which allow for direct fitting of the crack length vs. cycles curve to obtain the FCGR. The ability to fit small and long crack growth curves for cracks growing in region I confirms that region I crack growth rate is governed by power law behavior. The FCGR results show that small cracks are faster, but the transition from region I to region II occurs at a specific fatigue crack growth rate for both small and long cracks. This results in an apparent shift in ΔK at the transition and points at inhomogeneous sampling as the reason for the lower threshold of small cracks. The accurate small crack growth rate measurements are combined with long crack growth rate measurements to calculate the fatigue life from initial discontinuity dimensions, which correspond to the fatigue life results that are experimentally obtained for smooth specimens.

1.0 INTRODUCTION

The fatigue crack growth rate curve of metallic alloys is usually divided into three regions: region I corresponds to the steep slope in the fatigue crack growth rate (FCGR) curve near the threshold. Crack nucleation and propagation in region I corresponds to stage I crack growth that occurs along favorably oriented slip planes, which results in a faceted or cleavage-like fracture surface appearance (Forsyth, 1963, 1961). Region II corresponds to a moderate linear slope in the FCGR curve. Crack propagation in region II corresponds to stage II, which occurs in the tensile mode and the fracture surface shows signs of plasticity (Forsyth, 1963, 1961). Region III is usually regarded as the steep slope in the FCGR curve prior to final failure of the specimen.

In 1963, Paris et al. empirically showed that the FCGR has a power law relationship with the stress intensity factor range, ΔK, for region II fatigue crack growth (Paris and Erdogan, 1963):

$$\frac{da}{dN} = C(\Delta K)^n \quad , \tag{1}$$

where *da/dN* is the fatigue crack growth rate and *C* and *n* are constants. Around the same time power law behavior was also considered for region III and higher exponents were used to characterize the steeper slope in region III (Laird and Smith, 1962; Liu and Iino, 1969; McEvily and Boettner, 1963; Paris, 1964). In 1980 Radhakrishnan also fitted region I FCGR data of steel from various sources with Eqn (1) and concluded that the exponent in region I was about 4 times the exponent in region II (although in the paper regions I and II are called stage IIa and IIb, respectively) (Radhakrishnan, 1980). Besides the changes in the slopes between the

three regions, Wilhem showed in 1967 that there is a knee, i.e. a change in exponent, in the region II fatigue crack growth rate curve when plotted on a double logarithmic scale. The knee in the FCGR curve corresponds to the initial formation of shear lips on the fracture surfaces (Wilhem, 1967). Stofanak et al. also observed a knee in the FCGR curve of an extruded aluminum alloy (Stofanak et al., 1983). They concluded that changes in the slope of the FCGR curve correspond to a change in micromechanism of fatigue crack growth. The change in slope between region I and region IIa appears to coincide with the fracture surface transition from broad faceted areas to rough, blocky, faceted areas. The change in exponent between region IIa to Region IIb corresponded to a change from faceted growth to striated growth. This transition was seen to occur when the reversed plastic zone size was similar to the subgrain dimension. Wanhill showed for aluminum alloy (AA) 2024 that there are three transitions in the FCGR curve up to ~10^{-7} m/cycle (Wanhill, 1988). Wanhill also concluded that changes in fracture surfaces topography are associated with the transitions in the FCGR curve (Wanhill, 1988). Hence, the different stages of crack growth correspond to the different regions in the FCGR curve. Wanhill indicates that the transitions between regions occur when the monotonic or cyclic plane strain plastic zone size become equal to characteristic microstructural dimensions (Wanhill, 1988). The first transition occurs when the cyclic plastic zone size is equal to the mean planar distance between dispersoids, the second transition occurs when the cyclic plastic zone size is equal to the subgrain and dislocation cell sizes and the third occurs when the monotonic plastic zone size is equal to the grain dimensions (Wanhill, 1988). Newman et al. used five linear segments and four clear transition points to describe the FCGR curve of AA7075-T6 obtained from middle tension specimens in the L-T direction (Newman Jr. et al., 1994). The multilinear FCGR curve runs from 10^{-11} m/cycle to 10^{-4} m/cycle and the first three transitions occur at $1{\cdot}10^{-9}$, $1{\cdot}10^{-8}$ and $6.4{\cdot}10^{-8}$ m/cycle, which correspond to the three transitions observed by Yoder et al. for several 7XXX-series aluminum alloys and by Wanhill for AA2024 (Wanhill, 1988; Yoder et al., 1982). The fourth transition occurs at $1{\cdot}10^{-6}$ m/cycle and denotes the transition to rapid, unstable crack growth that is traditionally referred to as region III.

Newman et al. used a look-up table to describe the FCGR curve, were the points in the table correspond to transition points (TP) in the FCGR curve. They used this approach because a multilinear curve was able to describe the FCGR data more accurately than a multi-parameter equation. However, Amsterdam et al. showed that a pivot point can be used to describe change in the slope of the FCGR curve (Amsterdam and Grooteman, 2016):

$$\frac{da}{dN} = \frac{da}{dN_{TP}} \left(\frac{\Delta K}{\Delta K_{TP}} \right)^{n_i}, \tag{2}$$

where da/dN_{TP} and ΔK_{TP} are the FCGR and stress intensity factor range at the transition point where the slope, n_i, is changing.

The secant and incremental polynomial method, as described in ASTM E647, are normally used to obtain FCGR from the a-N curve (ASTM: E647-15, 2015). However, these methods result in noise in the FCGR curve and the amount of noise depends on 1) the method applied, 2) the error in the crack length measurement technique and 3) the crack length measurement frequency (Amsterdam, 2017; Amsterdam and Nawijn, 2018). In this paper we state that fatigue crack growth is governed by power law behavior at all crack lengths and all ΔK values. To accommodate for changes in the FCGR when there is a transition in crack propagation mechanisms, mathematical pivot points are introduced in the FCGR equation. The power law behavior and the introduction of pivot points allow for direct fitting of the a-N curve for long and small cracks to obtain the FCGR as function of ΔK. The advantage of directly fitting the a-N curve is that i) there is no noise in the resulting FCGR curve and ii) it is not necessary to fit noisy FCGR data with a model, because an exact description of the crack growth rate is known from the fit of the a-N curve. The accurate small and long FCGR data that is obtained using this method is used to predict and compare the fatigue life of smooth round stress-life (S-N) coupons with experimental results.

2.0 MATERIALS AND METHODS

2.1 Long crack specimen

Constant amplitude (CA) fatigue crack growth tests were performed on middle tension (M(T)) specimens at different maximum stress (S_{max}) and different stress ratios (R=S_{min}/S_{max}). M(T) specimens with dimensions of 500 mm x 160 mm were removed from aluminum alloy (AA) 7075-T7351 plate material with a thickness of 6.35 mm. The rolling direction was in the length of the specimens, hence loading-crack growth was in the L-T direction. Fatigue crack growth starter notches were central holes (1.6 mm diameter) with 0.7 mm deep electric discharge machined (EDM) slots on either side of the hole (total starter notch length of 3 mm). The EDM wire thickness was 0.16 mm. The area next to the starter notch was polished for optical crack growth measurements on both front and rear sides of the specimens. A constant amplitude 13.5 Hz sinusoidal load was introduced by a servo-hydraulic test machine with a 200 kN load cell. CA loading with the same maximum stress and stress ratio as for the actual test was used for pre-cracking the M(T) specimen to a single side crack length, a, of about 2 mm. The actual crack length after pre-cracking was measured with an optical travelling microscope.

Holes were drilled at 8 mm above and below the starter notch hole for copper pins. These were used for automated crack length measurements by direct current potential drop (DCPD). The current was introduced to the specimen at the specimen clamping. The potential drop of the specimen and a reference specimen was measured every 9 seconds by Matalect DCM-2 equipment using 12 readings and 11 samples. Potential drop data acquisition occurred every 100 or 200 cycles depending on the estimated number of cycles to failure. The DCPD data was converted to crack length data using Equation A2.5 in ASTM E647 (ASTM: E647-15, 2015). V_r in Equation A2.5 in ASTM E647 was adjusted for each specimen such that the crack length from the DCPD measurements at the start of the test is equal to the crack length measured with the optical travelling microscope after pre-cracking. High resolution photographs of the front and rear side of the specimen with length markers were taken during initial tests to verify the DCPD measurements. The tests were performed in lab air environment.

The stress intensity factor range, ΔK, for the M(T) specimens is calculated by:

$$\Delta K = \beta(a)\Delta S\sqrt{\pi a} \ , \tag{3}$$

where ΔS is the stress range during the test and β the Feddersen final width correction that is calculated according to ASTM E647 (ASTM: E647-15, 2015):

$$\beta = \sqrt{\sec\left(\frac{\pi a}{W}\right)} \ , \tag{4}$$

where W is the width of the specimen. The effective stress intensity factor range, ΔK_{eff}, is calculated using the Schijve crack closure correction (Schijve, 1986, 1981):

$$\Delta K_{eff} = (0.55 + 0.33R + 0.12R^2)\Delta K \tag{5}$$

2.2 Small crack specimens

Flat dogbone specimens were machined from the same 7075-T7351 plate as the M(T) specimens and tested with alternating CA and variable amplitude (VA) bands for quantitative fractography of small cracks. The CA bands consisted of 5000 high stress ratio CA cycles (R=0.77) and the crack dimensions and growth in a single band were determined in the scanning electron microscope (SEM) after failure of the specimen. Approximately 500 blind holes have been machined on the both sides of the plate material (1038 in total per specimen). The blind holes act as seeded defects for nucleation of surface cracks. The blind holes have been machined using

an ultrashort pulse laser with a pulse length of 10 ps and a wavelength of 532 nm, operated at 10 kHz pulse repetition frequency. The holes were machined by scanning the laser in layers of several concentric circles. Multiple layers were used to machine the holes to a depth of about 80 µm. Rows of blind holes were made perpendicular to the loading direction and a spacing of 2 mm was used within a row. Separation of the rows in the direction of loading was 0.5 mm and adjacent rows were staggered by 1 mm to minimize interaction between growing cracks.

The crack depth (a) at the deepest point was used to calculate ΔK. The geometry factor β for the surface cracks has been determined with AFGROW software for the deepest point of the surface crack as fraction of the thickness (t) using the measured crack dimensions (crack depth (a) / half of the surface length (c) ratio). The resulting geometry factor β is only applicable for these seeded defects:

$$\beta = 0.5599(a/t)^3 - 0.0953(a/t)^2 + 0.2034(a/t) + 0.5687 \qquad (6)$$

2.3 Smooth round S-N coupons

Smooth round coupons for stress-life testing were machined from 12.7 mm 7075-T7351 plate from the same mill. The coupons have a diameter of 3 mm and a reduced section length of 18 mm. The coupons have a stress concentration factor of unity (K_t=1) and were polished to a roughness of R_a<0.2 µm. A constant amplitude 25 Hz sinusoidal load was introduced by a servo-hydraulic test machine with a 100 kN load cell. A stress ratio of 0.1 was applied.

S-N curves are typically plotted with the cycles to failure on the horizontal axis and the stress on the vertical axis. However, since the cycles to failure is the outcome of the test and the maximum stress is the input value, in this paper the independent variable stress is plotted on the horizontal axis and the dependent variable on the vertical axis. This is especially important when regression analysis is used to obtain a power law exponent by minimizing the error between the model and the *dependent* variable. Plotting it vice versa results in incorrect fitting parameters.

2.4 Fractography

A FEI field emission gun (FEG) SEM was used for fractography on all three specimen types and energy dispersive analysis of X-rays (EDX) was used in the SEM to measure the composition of constituent particles on the fracture surface.

2.5 Fitting methodology

Making use of Eqn (2), the crack length, a, was fitted as function of cycles, N, using the following equation:

$$a(N) = a(0) + \sum_{j=0}^{N-1} \frac{da}{dN_i} \left(\frac{\Delta K_j}{\Delta K_i}\right)^{n_i}, \qquad (7)$$

where ΔK_j is the stress intensity factor range during the j^{th} cycle. For a constant stress range test ΔK_j is a function of the crack length at the j^{th} cycle, a_j. The pivot points in the FCGR curve are located at the coordinates (da/dN_i, ΔK_i) and the suffix i denotes the pivot point number. The pivot points correspond to the locations where the slope changes in the FCGR curve. In the fitting procedure the error between the measured crack lengths and the crack lengths calculated by Eqn (7) are minimized in a least square fitting procedure by changing the coordinates of the pivot points, the crack growth rates at the start and the end of the measurement, and the number of pivot points.

The pivot point coordinates fully define the slopes in between two pivot points. The crack growth rates at the start and the end of the measurement are required to define the slopes towards the first and after the last pivot point, respectively.

The error, ϵ, between the model (Eqn (7)) and each data point of the measured a-N curve is calculated as follows:

$$\epsilon = \sum_{j \in S} \left(\tilde{a}_j - a_j \right)^2 , \tag{8}$$

where a_j and $\tilde{a}_j$ are the measured and modelled crack lengths at the j^{th} cycle respectively. The set S contains the cycles at which a measured crack length was stored.

When calculating Eqn (7), to find the crack growth rate at ΔK in between two transition points either of the adjacent transition points may be used along with the slope at ΔK. For ΔK smaller than ΔK_1, the first slope, n_1, is used with ΔK_1, for ΔK larger than ΔK_1, the last slope, n_{i+1}, is used with ΔK_i.

3 RESULTS

3.1 Long crack growth rate measurements

Figure 1 shows a-N curves of two specimens that are tested at S_{max}=80 MPa and R=0.1. The crack lengths measured with DCPD show good agreement with the optical crack length measurements. The noise on the DCPD measurement is clearly visible due to the large amount of data points. The scatter in the optical measurements is less clear due to the limited number of measurements. The DCPD measurements are used to obtain the FCGR by fitting the DCPD a-N curves with Eq. 7. Figure 2 shows the normalized error between the DCPD a-N curve and the fit as a function of the number of slopes in the FCGR curve. Note that the number of slopes is one more than the number of transition points in a FCGR curve. The absolute value of the error depends on the number of data points, which depends on the test parameters. Therefore, the error of each specimen is normalized by the error at which the error does not significantly decreases anymore with increasing number of slopes. It is clear that the error does not decrease significantly when more than four slopes are used for specimen P1R2N2, and more than five for specimen P1R4N2 that is tested with a different stress ratio. When less than four or five slopes are used, the error between the fit and the measured a-N curve increases significantly. For specimen P2R3N1, which is tested at S_{max}=100 MPa and R=0.28, the number of slopes is less obvious and four or five slopes can be used the fit the a-N curve of this specimen.

Figure 3a shows the crack length vs. cycles curve of several specimens tested at different maximum stress and different stress ratios. The colored dots represent the crack lengths measured with DCPD and the solid white line represents the best fit of Eqn (7) for each specimen. The black markers in the white line represent the transition points that correspond to the least number of transition points and slopes that are necessary to obtain a small error between the fit and the measured a-N curve. All fits run right through the DCPD crack length data points and show good agreement with the shape of the curve, also at small crack lengths. Figure 3b shows the resulting FCGR as a function of ΔK (dashed lines). Multiple changes to the slope can be observed and the transitions from one slope to the next occur at specific FCGRs for all curves. The shapes of the FCGR curves are similar and the horizontal shift between the individual curves originates from the difference in stress ratios, as is shown by plotting the FCGR as function of ΔK_{eff} (solid lines). Since the FCGR of specimens P2R2N1, P2R1N7 and P1R4N2 at the start of the test are less than that of specimens P1R2N2 and P2R3N1, they require an additional transition point and slope at the beginning of the FCGR curve. For the FCGR range between $3 \cdot 10^{-9}$ and 10^{-5} m/cycle a minimum of four transition points and five slopes are necessary to obtain accurate fits for all specimens.

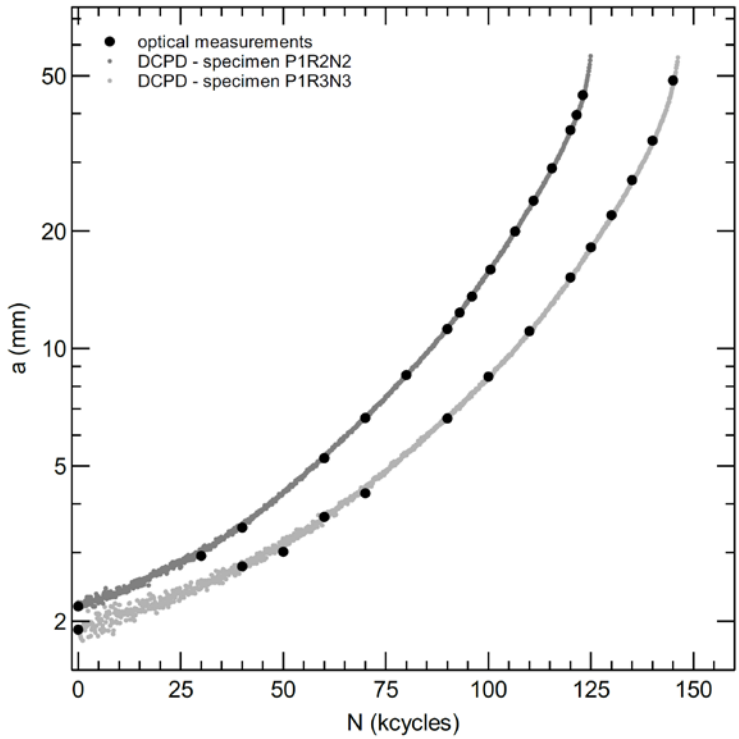

Figure 1 Crack length vs. cycles (a-N) curve for two M(T) specimen tested at S_{max}=80 MPa and R=0.1. The grey points indicate the crack length measurements using DCPD and the larger black dots indicate the optical crack length measurements

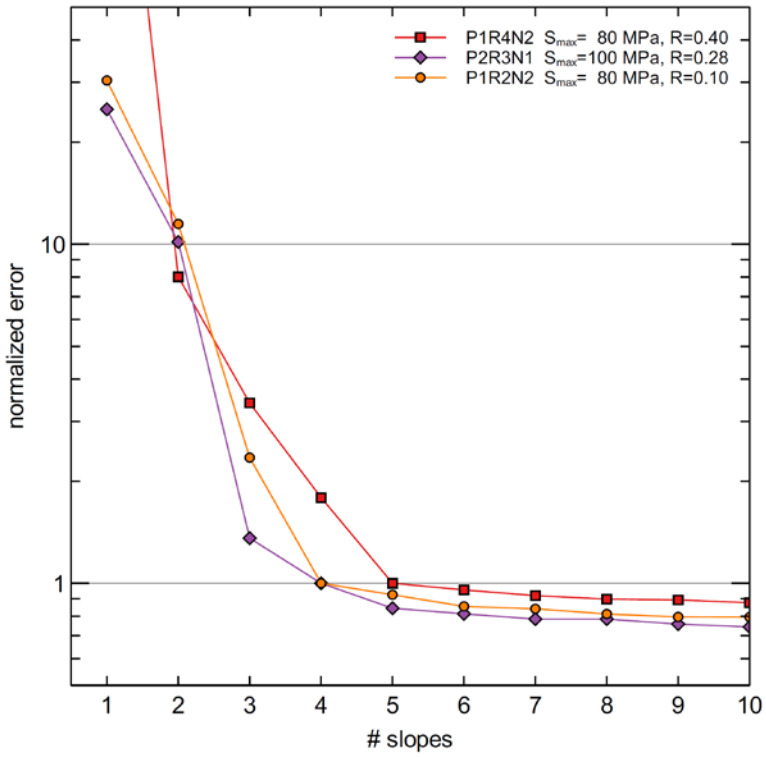

Figure 2 Normalized error between the measured a-N curve and the fit using Eqn (7) as function of the number of slopes in the FCGR curve

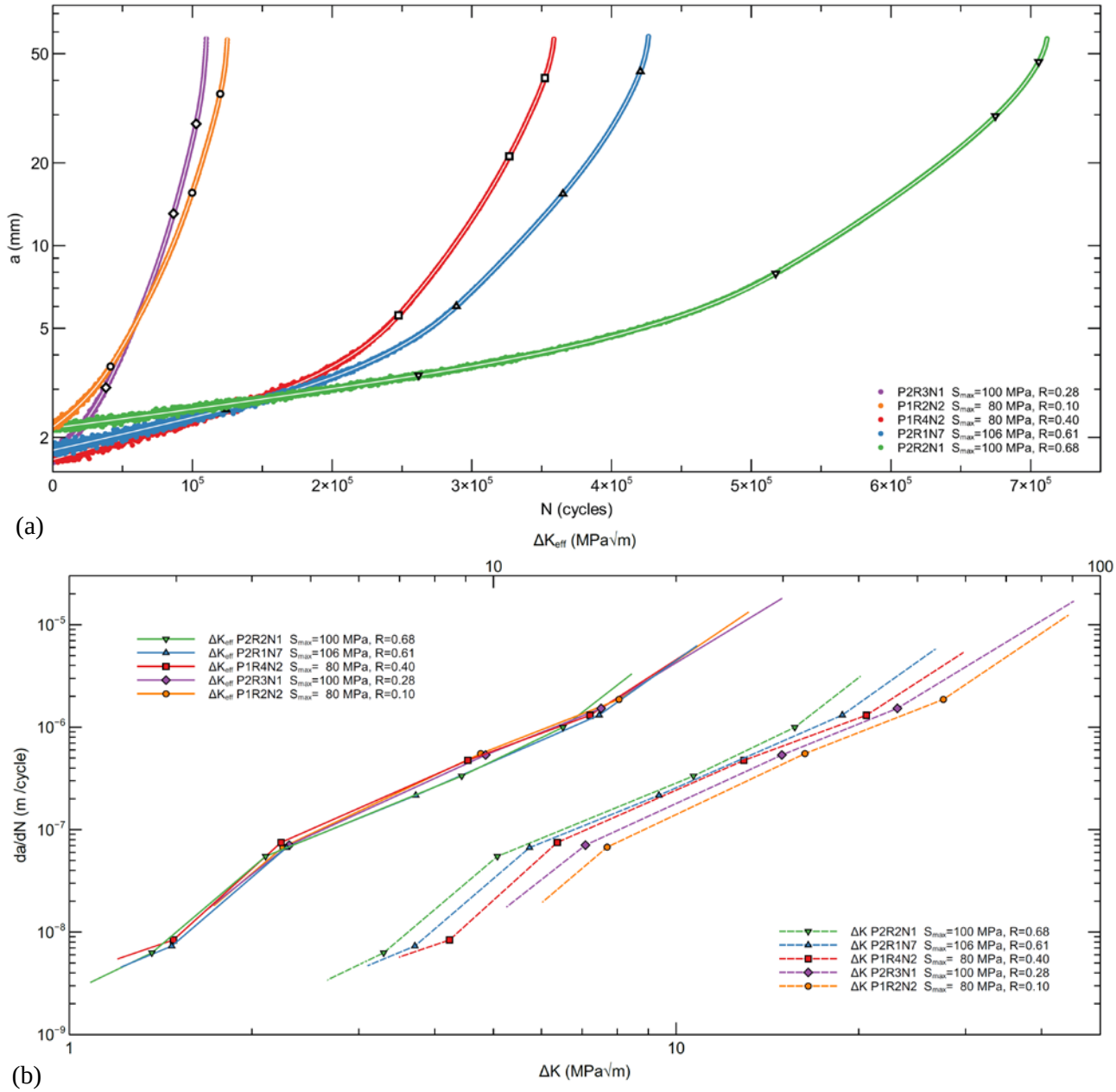

Figure 3 (a) Crack length vs. cycles (a-N) curves for M(T) specimens tested at different S_{max} and R. The white lines indicate the fit using Eqn (7) and the black symbols in the white lines indicate transitions points. (b) FCGR as a function of ΔK (bottom) and ΔK_{eff} (top). The transition points are indicated by symbols

Since specimen P2R3N1 has a similar FCGR range as specimen P1R2N2, the same number of slopes has been used to fit the a-N curve. The same fitting procedure can be used to fit the a-N data of a specimen tested with a very small constant stress range. Since the entire curve is fitted with Eqn (7), noise in the crack length measurement at very low FCGR ($<10^{-10}$ mm/cycle) does not influence the results. Figure 4 shows the a-N curve for a naturally increasing ΔK test with initial FCGRs of $< 10^{-10}$ m/cycle. The a-N curve can be fitted just as easily as a-N curves of specimens tested with higher stress ranges and higher crack growth rates. The insert shows the result of the fit and the FCGR at the start of the test is $5.8 \cdot 10^{-11}$ m/cycle. The FCGR increases quickly with increasing ΔK until the slope changes at $8.7 \cdot 10^{-10}$ m/cycle. The exponent of the initial slope is 8.43 and failure of the specimen at the end of the curve occurs by net-section overload.

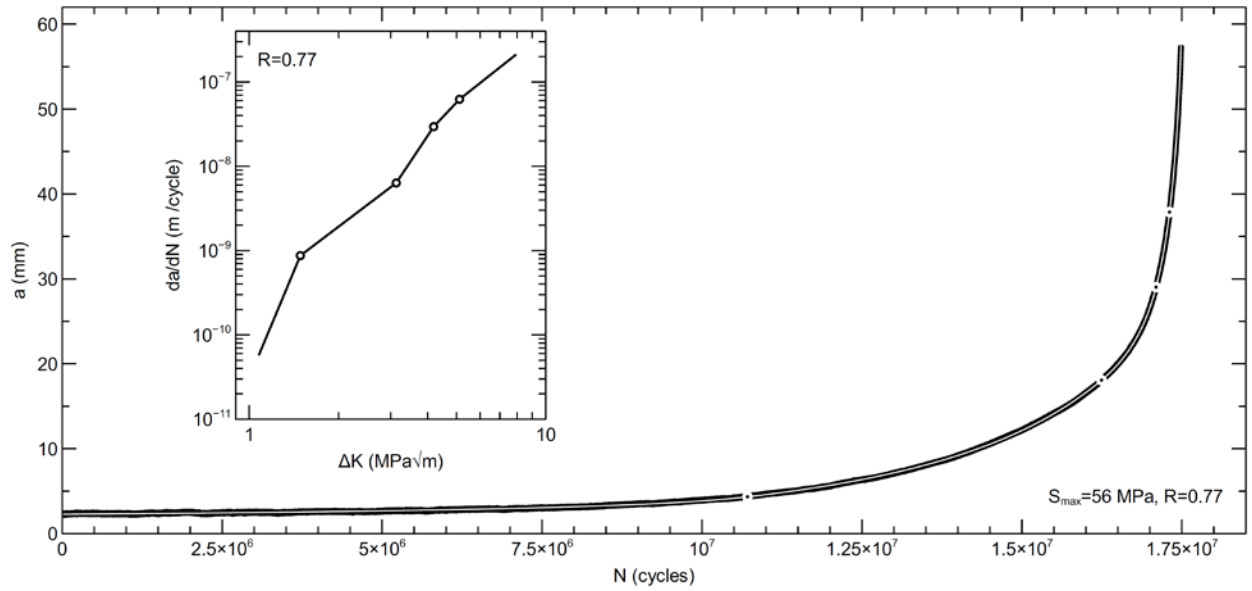

Figure 4 a-N curve for an long crack specimen tested at a small stress range. The white line indicate the fit using Eqn (7) and the white symbols in the white line indicate transitions points. The insert shows the resulting FCGR as a function of Δ*K*

3.2 Small crack growth rate measurements

Figure 5 shows the fatigue crack growth rate obtained from a small crack by alternating constant amplitude (*R*=0.77) and variable amplitude markerbands. The open dots represent FCGRs that are obtained from measuring the width of the CA bands, while the solid line represent the results from the crack depth vs. cycles fit, similarly as for the long crack specimens. The exponent of the steep slope of the small crack in region I is 12.8, which is greater than the exponent of the long crack in region I (n_1=8.43). The second slope of the small crack is slightly lower than that of the long crack such that the two curves for small and long cracks coincide near the transition to the third slope at a crack depth of about 2.2 mm.

3.3 From crack growth rate to fatigue (crack growth) life

Figure 6 shows S-N measurements for 7075-T7351 smooth round coupons for R=0.1, along with the calculated fatigue life. The calculated fatigue life is determined by a crack growth calculation (CGC) from the initial crack depth to final failure using appropriate stress intensity factor (SIF) solutions and small & long FCGR data. In the subsequent paragraphs the input for the CGC, i.e. initial crack depth, SIF solutions, FCGR data and final failure criteria, are given.

Fractography and EDX measurements indicate that for 75% of the coupons the fatigue cracks nucleated from constituent particles at the surface, 2% from internal pores and 23% from machine tool markings on the surface, even though the coupons were carefully machined and polished. From the constituent particles 5% failed from Al_2O_3 phases, 18% from Mg_2Si phases and 77% from Fe-containing phases. The initial discontinuity dimensions (IDD) is defined as the actual dimensions of a single initial discontinuity. The Fe-containing particles at the surface are one of the initial discontinuities and in this case the IDD is regarded as the maximum depth of the particle as measured from the surface. The IDD of the majority of the Fe-containing phases ranges between 12 and 24 μm. The coupons with Fe-containing constituent particles having an IDD in the order of 12 μm, 16 μm or 24 μm are indicated separately in Figure 6. Figure 7 shows an SEM image with an example of crack nucleation from an Fe-containing constituent particle with an IDD of 17.7 μm.

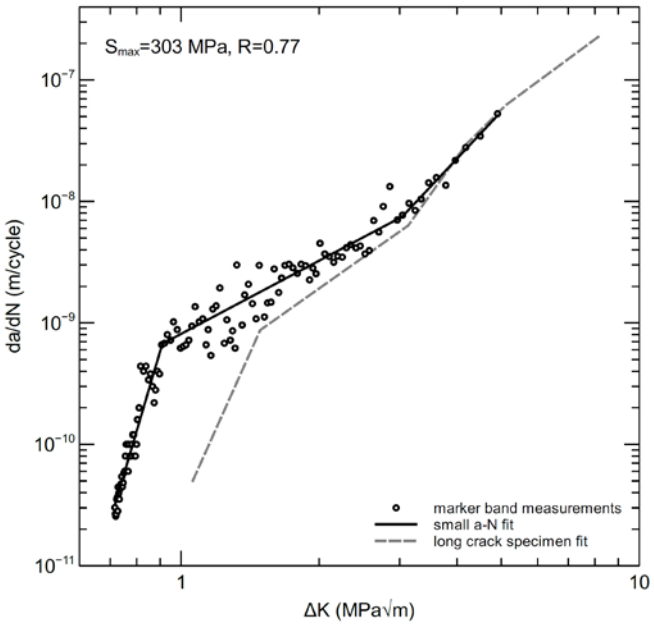

Figure 5 Small crack growth measurements and small crack depth vs. cycles fit. The long crack specimen fit corresponds to the specimen in Figure 4

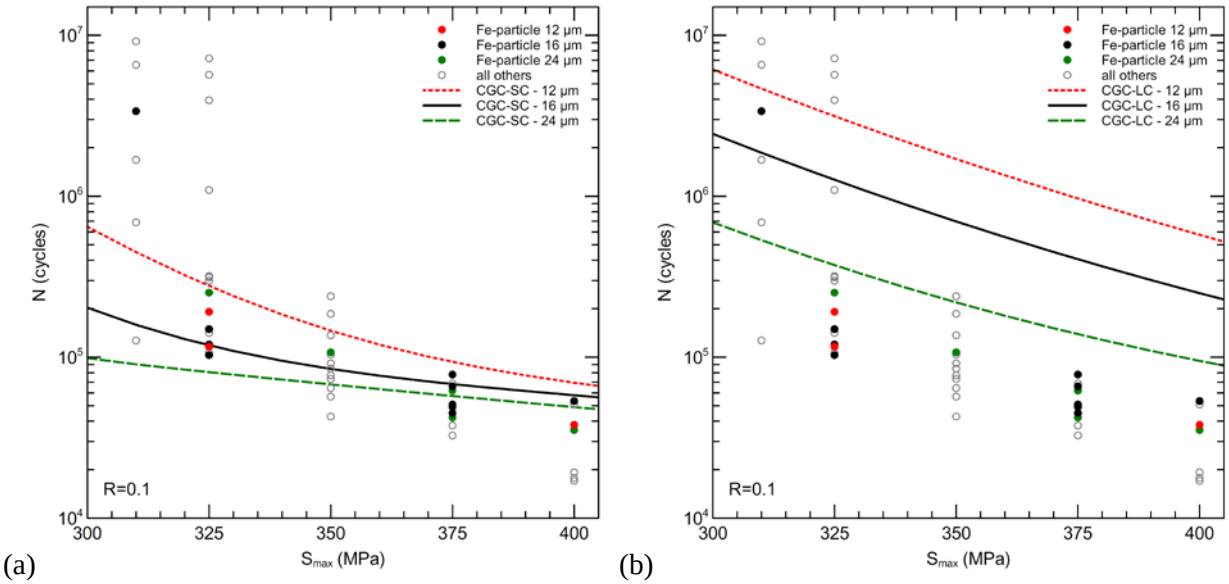

Figure 6 Measured fatigue life as a function of the maximum stress for R=0.1 and predicted fatigue life using (a) small crack (SC) and (b) long crack (LC) growth rate data. The filled dots represent specimens that nucleated a crack from Fe-containing constituent particles with IDD in the order of 12 µm, 16 µm or 24 µm. The lines indicate the crack growth calculation (CGC) for initial crack depths of 12 µm, 16 µm or 24 µm

Fractography also showed that the crack shape during crack growth is characterized by a circular crack front with the center of the circle at the surface of the specimen and the origin of the crack. Toribio et al. give an overview of SIF solutions for surface cracks in round bars subjected to tension loading (Toribio et al., 2009). The SIF solutions by Astiz and by Carpinteri for circular cracks in round bars are similar for $a/D \geq 0.1$, where a is the crack depth and D the diameter of the bar (Astiz, 1986; Carpinteri, 1992). However, for $a/D < 0.1$ the

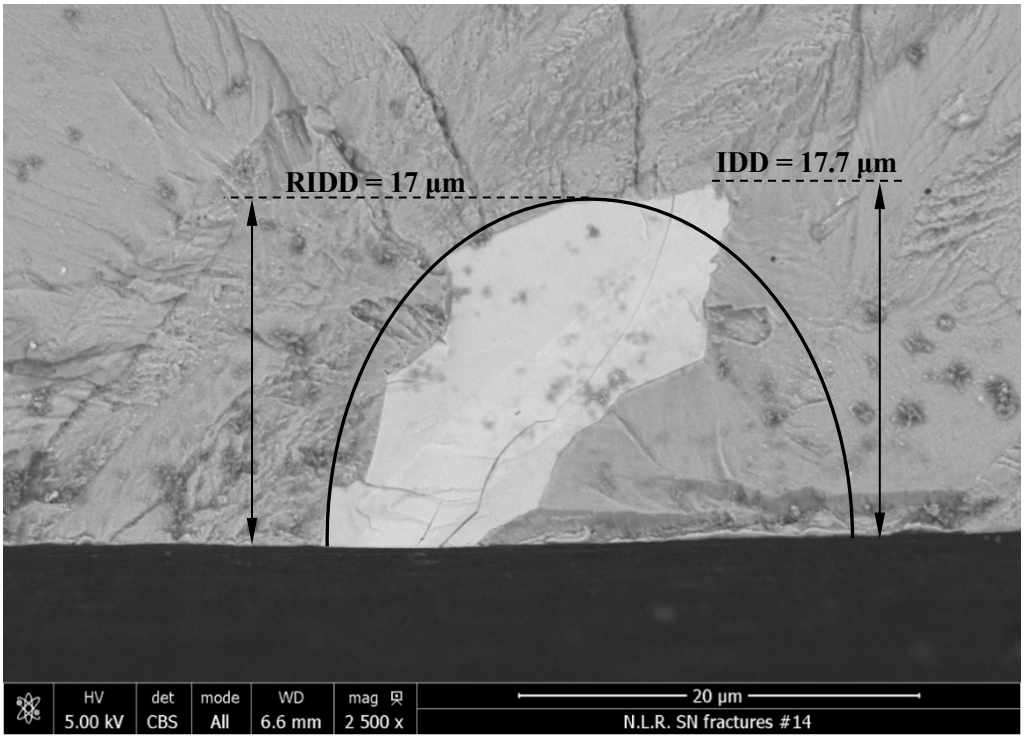

Figure 7 SEM image of an Fe-containing constituent particle from which crack nucleation occurred. The black ellipse has a depth of 17 µm and an *a*/*c* ratio of 1.29

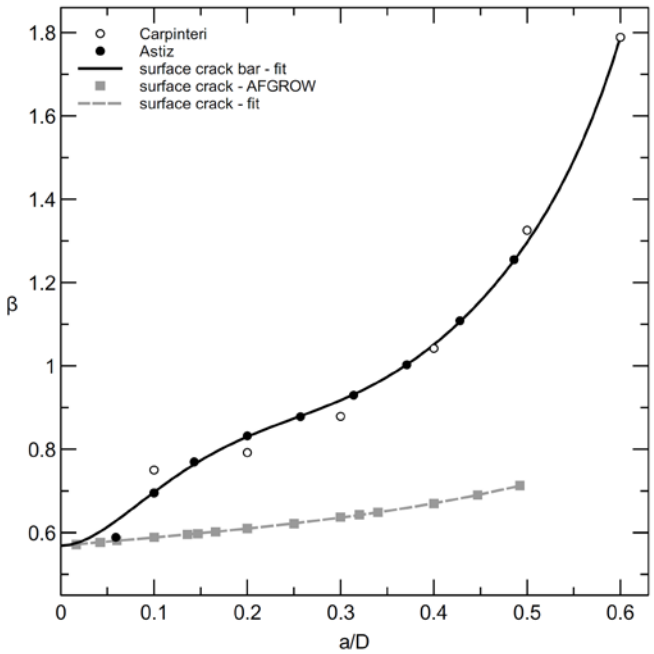

Figure 8 Geometry factor, *β*, for a round bar as a function of the surface crack depth to diameter ratio, Eqn (9). For the surface crack in a rectangular cross-section, the thickness *T* is used for *D*

two solutions start to deviate. The value of β goes to 0.74 for the solution of Carpinteri and to 0.35 for the solution of Astiz when a/D goes to zero (Toribio et al., 2009). However, the lowest a/D that was used by Astiz to determine the SIF solution was 0.059, which resulted in a β of 0.59. This value is close to the value for a surface crack in a plate with $a/t=0$ (see Eqn (6)). For $a<<D$, it is expected that the influence of the curvature is

very small and the SIF solution should approach the SIF solution of a surface crack in a plate. To avoid systematic errors between the determination of small crack FCGR measurements and the small crack growth calculation, a β value of 0.5687 was used for a/D=0. This means that β is similar as the β for which the crack growth data was obtained and possible effects from the plane stress situation at the surface on the crack shape for $a<<D$ is accounted for. When the crack depth increases, the influence of the diameter curvature increases and the solutions of Astiz and Carpinteri are used, see Figure 8. The following polynomial is used to describe β for the smooth round coupons and $0<a/D\leq 0.6$:

$$\beta = 362.6\left(\frac{a}{D}\right)^6 - 683.6\left(\frac{a}{D}\right)^5 + 507\left(\frac{a}{D}\right)^4 - 174.3\left(\frac{a}{D}\right)^3 + 26.15\left(\frac{a}{D}\right)^2 - 0.02846\frac{a}{D} + 0.5687 \quad (9)$$

In the CGC the crack growth rate at the deepest point, i.e. the crack depth (a), is calculated and it is assumed that the circular shape of the crack is maintained for $a/D>0.1$. For $a/D<0.01$, Eqns (6) and (9) are similar and the influence of the curvature of the bar diameter is small. This implies that the a/c ratio should be similar to that of small surface cracks, which is 1.29. For the constituent particle in Figure 7 a crack depth of 17 µm and an a/c ratio of 1.29 characterizes the shape of the particle well. The initial crack depth and a/c ratio that represents the shape and dimensions of the initial discontinuity is referred to as the representative initial discontinuity dimension (RIDD). If the a/c ratio is incorporated in the geometry factor, β, the RIDD only consists of a crack depth. The RIDD is used as initial crack depth in the CGC.

Figure 9 shows the FCGR as function of ΔK_{eff} for all long crack specimens. This long crack master curve consists of 54 specimens with 11 different maximum stresses and 13 different stress ratios. The master curve shows that there are five transition points and six slopes between FCGR of $5.8\cdot10^{-11}$ and 10^{-5} m/cycle. The red line indicates the FCGR and pivot points for the small crack growth calculation and is a combination of the small FCGR measurement of Figure 5 and the long FCGR master curve. The effective stress intensity range is used to obtain the crack growth rates at R=0.1. To obtain the red line in Figure 9 the first slope in region II

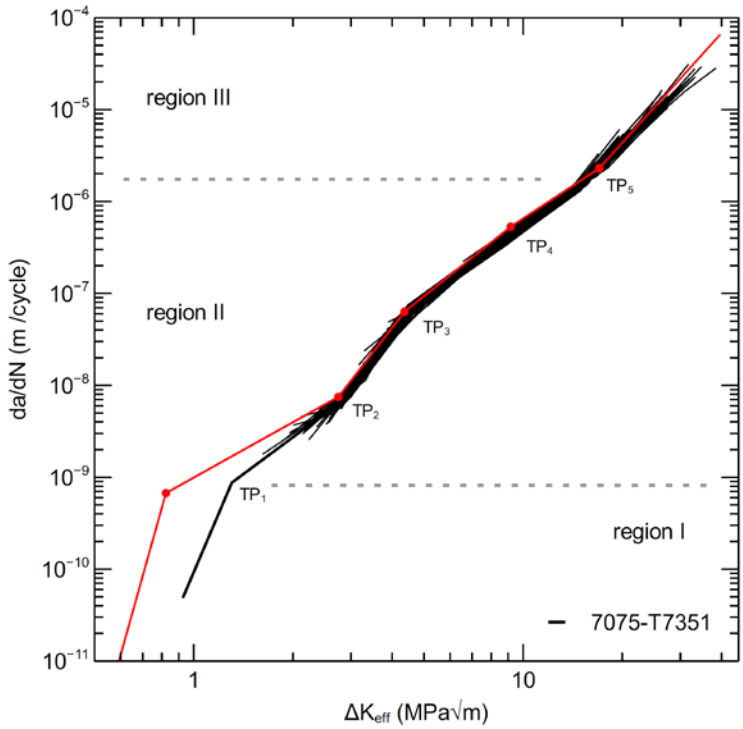

Figure 9 Long FCGR master curve as a function of ΔK_{eff} with indications for the transitions points. The master curve consists of 54 specimens with 11 different maximum stresses and 13 different stress ratios. The red line indicates the FCGR and pivot points for the small crack growth calculation and is a combination of the small and long FCGR measurements

was extended till it intersects with the R=0.1 long crack growth data of Figure 9. From that point onwards the R=0.1 long crack data is used for the red line. For the long CGC the same data (red line) is used, except the first transition point (TP_1) and the first two slopes of the long FCGR master curve are used.

The CGC is ended when the net-section stress reaches the ultimate tensile strength of the material or when the maximum SIF reaches the fracture toughness (K_{IC}). All specimens in the calculations failed by net-section overload and the final crack depths in the calculation corresponded well with the measured crack depths (see Figure 10).

There is a good agreement between the calculated fatigue lives and the measured fatigue life of the coupons for $310>S_{max}>375$ MPa when the small FCGR data and three different RIDDs are used (see Figure 6). When the long FCGR data is used the prediction overestimates the fatigue life for all three RIDDs.

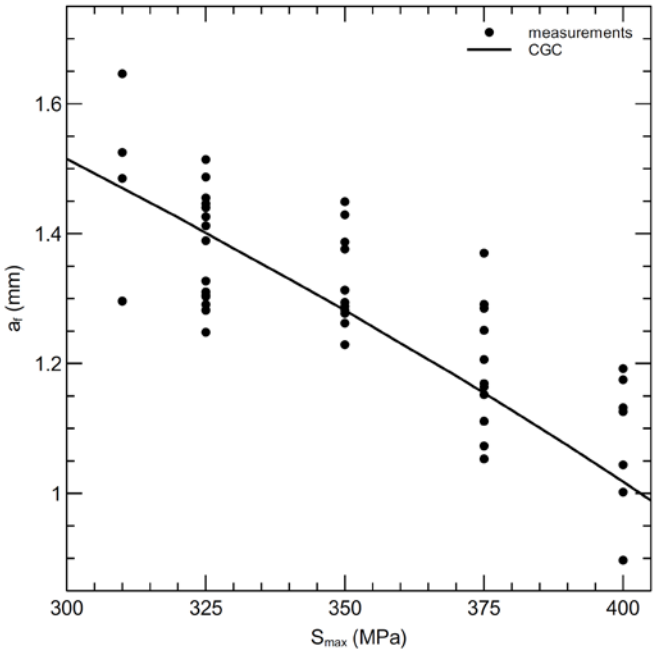

Figure 10 Crack depth at failure as a function of the maximum stress for the smooth round S-N coupons (R=0.1)

4 DISCUSSION

Figure 3 - Figure 5 show that the fitting method is applicable for small and long crack growth curves and results in accurate FCGR curves that are suitable for the exact reconstruction of the measured a-N curves. The ability to fit small and long crack growth curves for cracks growing in region I confirms that region I crack growth rate is governed by power law behavior. The method can also be used on a-N curves of variable amplitude (VA) loading to obtain VA FCGRs (Amsterdam, 2020).

4.1 Long and small crack growth rate behavior

Small cracks are faster than expected from long crack growth rate data (Pearson, 1975). For long cracks the crack width and length are much larger than the microstructural length scales and generally linear elastic fracture mechanics (LEFM) can be applied (Ritchie and Lankford, 1986). Short cracks are small in one dimension, but large in another (Ritchie and Lankford, 1986), such as a through crack that nucleates from a notch. Small cracks are small in all dimensions and in literature distinctions are made between

microstructurally, mechanically and physically small cracks to explain why small cracks can grow at higher growth rates than long cracks. (Ritchie and Lankford, 1986; Suresh and Ritchie, 1984). Microstructurally small cracks (MSC) have dimensions comparable to the scale of the microstructure and the plastic zone size is less than important microstructural features such as the distance between dispersoids, the subgrain and dislocation cell sizes or the grain size (Ritchie and Lankford, 1986). The growth of MSC is highly affected by local microstructural characteristics and environment (Messager et al., 2020; Murakami and Endo, 1994; Suresh and Ritchie, 1984; Taylor, 1992; Yoshinaka et al., 2019). The crack is able to grow in a preferential location and orientation and the crack front covers only one or several grains, so that the crack growth is not averaged with less advantageously oriented grains (Ritchie and Lankford, 1986). This inhomogeneous sampling of the microstructure probably plays a major role in the distinction between small cracks and short through-thickness cracks, whose crack fronts must encompasses many grains (Ritchie and Lankford, 1986).

Figure 9 shows that all long FCGR curves collapse on a master curve for ΔK_{eff} and it is equivalent to state that the transition points TP_1-TP_5 occur at a specific ΔK_{eff} or a specific FCGR. Figure 5 shows the evolution of the FCGR as function of ΔK for a MSC and a long crack. The results were both obtained with constant ΔS testing, so with naturally increasing ΔK testing, and with the same stress ratio (R=0.773). Therefore, the figure would look the same if the FCGR was plotted as function of ΔK_{eff}. The MSC shows faster FCGR compared to the long crack, which is consistent with literature. The slopes of the small crack in regions I and II are different compared to the long crack. However, Figure 5 and Figure 9 show that the transition from region I to region II for the MSC occurs at the same FCGR as for the long crack. The FCGR of the MSC is obtained by the small crack length fit using Eqn (7) and hence the transition point from region I to region II can be accurately determined. Since the transition from region I to region II (TP_1) for small and long cracks occurs at a specific FCGR, it is concluded that the transition from region I to region II is governed by the FCGR instead of the crack driving force, ΔK_{eff}. Hence, regions I, II and III in Figure 9 are indicated by horizontal dashed lines at specific FCGRs. One might argue that crack-closure is not present in the small crack when it is an MSC, but it is also expected that limited crack closure is present in the long crack for R=0.773. Even when no closure is assumed for the small crack and closure is assumed for the long crack, there is still a gap in ΔK_{eff} at the transition TP_1.

The long FCGRs originate from through cracks in M(T) specimens that span many grains in the 6.35 mm thickness of the plate and the location of the crack is pre-determined by the location of the 3 mm long EDM notch. In region I the crack front runs across many grains and remains in a plane normal to the uniaxial applied stress. Hence, the crack growth rate of long cracks is an average over many cycles and many grains. Consequently, it has been referred to as stage I-like propagation (Petit and Kosche, 1992). The MSC propagate in only a few grains and many crack nucleation and propagation locations are present in a single specimen. For a transition from region I to region II at a specific FCGR, the difference between the region I FCGR of fast small cracks and average long cracks result in an apparent shift in ΔK_{eff} at which the transition occurs. Once it is assumed that the transitions between regions is controlled by the FCGR in conjunction with the microstructural features, a lower threshold becomes the direct result of the presence of variability in MSC FCGR. If the microstructure is locally very beneficial for a small crack growing in stage I this will give a high FCGR constant. Since the MSCs that are measured are always the fastest ones, the threshold of the MSC will shift to smaller values compared to the long crack threshold. This confirms inhomogeneous sampling as the reason for the lower threshold for small cracks.

In literature this shift is often referred to as the shift in $\Delta K_{threshold}$. Kitagawa and Takahashi were the first to show that the threshold for short cracks actually decreased with decreasing crack length and the threshold stress approached the smooth bar fatigue limit for MSC (Kitagawa and Takahashi, 1976; Suresh and Ritchie, 1984). The Kitagawa-Takahashi diagram addresses the higher crack growth rate for small cracks by an empirical relationship that shifts the threshold for small initial crack lengths, but it does not give a physical explanation. Adjustments to the diagram have been proposed by El haddad et al. by adding a fictitious crack length to the physical crack length (El Haddad et al., 1979) and Murakami et al. by replacing the crack length by the square root of the area (Murakami et al., 1989; Murakami and Usuki, 1989). However, it is still

deterministic in a sense that cracks either grow or do not grow depending on which side of the curve they are located based on their length or area and stress. However, there is enough evidence that small cracks do lead to failure, while they are in the no-grow area and vice versa (Persenot et al., 2020). Addressing the problem with probabilistics with proper distributions for the initial crack length and for the variability in small FCGR should be able to account for this. It is also capable of explaining the scatter that is observed in S-N curves and explain the size effect, i.e. the difference in fatigue life in large specimens or components compared to that of small specimens. This is also for notches, where a large and small hole can have the same stress concentration factor (K_t), but the volume of material in the high stress region is very different. Once a crack nucleates at a suitable location at the edge of the large hole, it grows longer in a high stressed region due to the higher radius/crack length ratio.

4.2 From crack growth rate to fatigue (crack growth) life

Forman was one of the first to investigate the use of fracture mechanics for crack nucleation from initial discontinuities (Forman, 1972). El Haddad et al. incorporated short crack effects to the fracture mechanics by adjusting the ΔK_{th} to predict the fatigue life of smooth and notched specimens (El Haddad et al., 1981). Herman et al. stated that it is possible to use long cracks with absence of closure effects at high stress ratios to predict the crack growth rates of small cracks and use that data to simulate S-N response of actual components (Herman et al., 1988). Newman et al. used one power law exponent in regions I & III and multiple exponents in regions II to calculate the S-N curve (Newman Jr., 1998; Newman Jr. et al., 2014, 2000, 1986). Newman used tabular data to represent the transition points and power law behavior was assumed between the transition points (Newman Jr. et al., 1994). The tabular data was obtained by visually drawing solid lines through the long crack growth rate data as function of ΔK_{eff} (Newman Jr. et al., 2000). Small crack growth rate data was used to establish the ΔK_{eff} for the transition from region I to region II and for the slope in region I. This data was used to calculate the S-N curve for a given RIDD. The same approach is followed here, with the exception that power law behavior is assumed a priori and the pivot points are determined by fitting the crack length vs. cycles curves of small and long cracks directly using multiple exponents (Eqn (7)). This results in accurate values for the pivot points and slopes of the small and long FCGR (see Figure 5). Figure 6 clearly shows that the CGC overestimates the fatigue life for all three RIDDs when long FCGR data is used. The CGC shows good agreement when accurate small FCGR data is used.

For the crack growth calculations it was assumed that the crack grew immediately from the RIDD and a nucleation phase was omitted. Barter et al. expected immediate fatigue crack growth from pre-cracked constituent particles under high cyclic stress and observations on crack nucleation from corrosion pits indicated that crack nucleation from less sharp stress concentrator occurs essentially immediate upon the application of cyclic loading (Barter et al., 2012, 2002; Molent et al., 2011; van der Walde and Hillberry, 2007). Therefore, it is expected that crack growth from pre-cracked or cracked Fe-containing particles occurs from the first loading cycle for highly loaded smooth S-N specimens. The predicted fatigue lives at maximum stresses greater than 350 MPa are greater than the experimental lives (see Figure 6). Adding additional cycles for nucleation would only increase the discrepancy between the predicted and experimental fatigue lives.

A digital twin of an aircraft is a digital model that combines the digital thread, i.e. all historical data of the aircraft including; geometry, production, modifications, maintenance, repair and service usage data, with degradation models in such a way that this creates a digital copy that represents the physical state of the aircraft. The ability to perform in-time inspections or maintenance based upon the information of a digital twin highly depends on the accuracy of the material degradation models that are used in the digital twin algorithms. The work in this paper can be used to obtain accurate small FCGR data, which is necessary to accurately predict the fatigue life of cracks nucleating from initial discontinuities that are naturally present in all engineering alloys. The current work is applicable for component locations with low stress concentration factors (K_t). Future work will focus on the expansion of this framework to high K_t locations, variable amplitude and probabilistics, such that the framework can be used to predict the fatigue life distribution for cracks nucleating from initial discontinuities for entire engineering structures under realistic loading conditions.

5 CONCLUSIONS

By introducing mathematical pivot points in the Paris equation it is possible to directly fit the crack length vs. cycles (a-N) curve to obtain the FCGR as function of ΔK. The fitting method results in accurate FCGR curves that are suitable for the exact reconstruction of the measured a-N curves. The ability to accurately fit a-N curves for microstructurally small and long cracks growing in region I confirms that region I FCGR is governed by power law behavior. The same applies for crack growth in region II and III, indicating that crack growth is governed by power law behavior in all regions. The results for constant ΔS testing and therefore naturally increasing ΔK testing of small and long cracks show that crack growth rates of small cracks in region I are faster. However, the transition from region I to region II occurs at a specific fatigue crack growth rate for both small and long cracks, which results in an apparent shift in ΔK at the transition. This points at inhomogeneous sampling as one of the reasons for the lower threshold of small cracks. The accurate small crack growth rates that are obtained using the new methodology are used to calculate the fatigue life from initial discontinuity dimensions. The calculated fatigue lives correspond to the experimental fatigue lives that are obtained for smooth S-N specimens with the same initial discontinuity dimensions.

CONFLICT OF INTEREST

The authors declare no conflict of interest.

AUTHOR CONTRIBUTION

EA was responsible for the set-up and execution of experimental work, data analysis and theoretical development and writing of the manuscript. MN was responsible for data analysis architecture and initial algorithms for data processing. JWEW performed further development of the algorithms for data processing and processed the crack length vs. cycles data.

ACKNOWLEDGEMENTS

This work was part of a public-private partnership project called “Prediction of fatigue in engineering alloys” (PROF). Financial contributions from the Netherlands Ministry of Economic Affairs and Climate Policy, through TKI-HTSM and the Materials Transition Programme, the Netherlands Ministry of Defence, GKN Fokker, Embraer, Airbus, Wärtsilä and Lloyd’s Register are highly acknowledged. Scientific discussions with Tim Janssen (GKN Fokker), Giorgia Aleixo, Marcelo de Barros (Embraer), Derk Daverschot (Airbus), Jiajun Wang, Aarif Zaheer (Wärtsilä), Weihong He, Li Xu (Lloyd’s Register), Jesse van Kuijk and René Alderliesten (TU Delft) are highly acknowledged.

REFERENCES

Amsterdam, E., 2020. Effect of Crack Length and Reference Stress on Variable Amplitude Fatigue Crack Growth Rate, in: Niepokolczycki, A., Komorowski, J. (Eds.), ICAF 2019 – Structural Integrity in the Age of Additive Manufacturing. Springer International Publishing, Cham, pp. 539–550. https://doi.org/10.1007/978-3-030-21503-3_43

Amsterdam, E., 2017. On the validity of the Paris equation, in: AIAC 2017: Innovation into Aerospace Future. Presented at the 17th Australian Aerospace Congress (AIAC17), Melbourne, Vic., pp. 1–6.

Amsterdam, E., Grooteman, F., 2016. The influence of stress state on the exponent in the power law equation of fatigue crack growth. International Journal of Fatigue 82, 572–578. https://doi.org/10.1016/j.ijfatigue.2015.09.013

Amsterdam, E., Nawijn, M., 2018. Fatigue tests for alloys. Aerospace Testing International Showcase 2018, 16–20.

Astiz, M.A., 1986. An incompatible singular elastic element for two- and three-dimensional crack problems. Int J Fract 31, 105–124. https://doi.org/10.1007/BF00018917

ASTM: E647-15, 2015. Test Method for Measurement of Fatigue Crack Growth Rates (No. ASTM E647), Annual Book of ASTM Standards. ASTM International, West Conshohocken, PA. https://doi.org/10.1520/E0647-15E01

Barter, S.A., Molent, L., Wanhill, R.J.H., 2012. Typical fatigue-initiating discontinuities in metallic aircraft structures. International Journal of Fatigue 41, 11–22. https://doi.org/10.1016/j.ijfatigue.2011.10.017

Barter, S.A., Sharp, P.K., Holden, G., Clark, G., 2002. Initiation and early growth of fatigue cracks in an aerospace aluminium alloy. Fatigue & Fracture of Engineering Materials & Structures 25, 111–125. https://doi.org/10.1046/j.1460-2695.2002.00482.x

Carpinteri, A., 1992. Elliptical-arc surface cracks in round bars. Fat Frac Eng Mat Struct 15, 1141–1153. https://doi.org/10.1111/j.1460-2695.1992.tb00039.x

El Haddad, M.H., Smith, K.N., Topper, T.H., 1979. Fatigue crack propagation of shorts cracks. Journal of Engineering Materials and Technology 101, 42–46.

El Haddad, M.H., Topper, T.H., Topper, T.N., 1981. Fatigue Life Predictions of Smooth and Notched Specimens Based on Fracture Mechanics. Journal of Engineering Materials and Technology 103, 91–96. https://doi.org/10.1115/1.3224996

Forman, R.G., 1972. Study of fatigue crack initiation from flaws using fracture mechanics theory. Engineering Fracture Mechanics 4, 333–345. https://doi.org/10.1016/0013-7944(72)90048-3

Forsyth, P.J.E., 1963. Fatigue damage and crack growth in aluminium alloys. Acta Metallurgica 11, 703–715. https://doi.org/10.1016/0001-6160(63)90008-7

Forsyth, P.J.E., 1961. A two stage process of fatigue crack growth, in: Crack Propagation: Proceedings of Cranfield Symposium. Presented at the Crack Propagation Symposium, Her Majesty's Stationery Office, Cranfield, pp. 76–94.

Herman, W.A., Hertzberg, R.W., Jaccard, R., 1988. A simplified laboratory approach for the prediction of short crack behavior in engineering structures. Fat Frac Eng Mat Struct 11, 303–320. https://doi.org/10.1111/j.1460-2695.1988.tb01183.x

Kitagawa, H., Takahashi, S., 1976. Applicability of fracture mechanics to very small cracks or the cracks in the early stage, in: Proc. of 2nd Int. Conf. Mech. Behaviour of Materials. Presented at the Int. conf. Mech. Behaviour of Materials, American Society of Metals, pp. 627–631.

Laird, C., Smith, G.C., 1962. Crack propagation in high stress fatigue. Philosophical Magazine 7, 847–857. https://doi.org/10.1080/14786436208212674

Liu, H.W., Iino, N., 1969. A mechanical model for fatigue crack propagation, in: Proceedings of the 2nd Int. Conference on Fracture. Presented at the 2nd Int. Conference on Fracture, Chapman and Hall, pp. 812-824 (paper 71).

McEvily, A.J., Boettner, R.G., 1963. On fatigue crack propagation in F.C.C. metals. Acta Metallurgica 11, 725–743. https://doi.org/10.1016/0001-6160(63)90010-5

Messager, A., Junet, A., Palin-Luc, T., Buffiere, J., Saintier, N., Ranc, N., El May, M., Gaillard, Y., King, A., Bonnin, A., Nadot, Y., 2020. In situ synchrotron ultrasonic fatigue testing device for 3D characterisation of internal crack initiation and growth. Fatigue Fract Eng Mater Struct 43, 558–567. https://doi.org/10.1111/ffe.13140

Molent, L., Barter, S.A., Wanhill, R.J.H., 2011. The lead crack fatigue lifing framework. International Journal of Fatigue 33, 323–331. https://doi.org/10.1016/j.ijfatigue.2010.09.009

Murakami, Y., Endo, M., 1994. Effects of defects, inclusions and inhomogeneities on fatigue strength. International Journal of Fatigue 16, 163–182. https://doi.org/10.1016/0142-1123(94)90001-9

Murakami, Y., Kodama, S., Konuma, S., 1989. Quantitative evaluation of effects of non-metallic inclusions on fatigue strength of high strength steels. I: Basic fatigue mechanism and evaluation of correlation between the fatigue fracture stress and the size and location of non-metallic inclusions. International Journal of Fatigue 11, 291–298. https://doi.org/10.1016/0142-1123(89)90054-6

Murakami, Y., Usuki, H., 1989. Quantitative evaluation of effects of non-metallic inclusions on fatigue strength of high strength steels. II: Fatigue limit evaluation based on statistics for extreme values of inclusion size. International Journal of Fatigue 11, 299–307. https://doi.org/10.1016/0142-1123(89)90055-8

Newman Jr., J.C., 1998. The merging of fatigue and fracture mechanics concepts: a historical perspective. Progress in Aerospace Sciences 34, 347–390. https://doi.org/10.1016/S0376-0421(98)00006-2

Newman Jr., J.C., Anagnostou, E.L., Rusk, D., 2014. Fatigue and crack-growth analyses on 7075-T651 aluminum alloy coupons under constant- and variable-amplitude loading. International Journal of Fatigue 62, 133–143. https://doi.org/10.1016/j.ijfatigue.2013.04.020

Newman Jr., J.C., Swain, M.H., Phillips, E.P., 1986. An assessment of the small-crack effect for 2024-T3, in: Small Fatigue Cracks. pp. 427–452.

Newman Jr., J.C., Wu, X.R., Swain, M.H., Zhao, W., Phillips, E.P., Ding, C.F., 2000. Small-crack growth and fatigue life predictions for high-strength aluminium alloys. Part II: crack closure and fatigue analyses. Fat Frac Eng Mat Struct 23, 59–72. https://doi.org/10.1046/j.1460-2695.2000.00242.x

Newman Jr., J.C., Wu, X.R., Venneri, S.L., Li, C.G., 1994. Small-crack effects in high-strength aluminum alloys - A NASA/CAE cooperative program (No. NASA-RP-1309).

Paris, P.C., 1964. The fracture mechanics approach to fatigue, in: Proc. of the 10th Sagamore Army Materials Research Conference. Syracuse University Press, pp. 107–132.

Paris, P.C., Erdogan, F., 1963. A critical analysis of crack propagation laws. Journal of Basic Engineering 528–533.

Pearson, S., 1975. Initiation of fatigue cracks in commercial aluminium alloys and the subsequent propagation of very short cracks. Engineering Fracture Mechanics 7, 235–247. https://doi.org/10.1016/0013-7944(75)90004-1

Persenot, T., Burr, A., Dendievel, R., Buffière, J.-Y., Maire, E., Lachambre, J., Martin, G., 2020. Fatigue performances of chemically etched thin struts built by selective electron beam melting: Experiments and predictions. Materialia 9, 100589. https://doi.org/10.1016/j.mtla.2020.100589

Petit, J., Kosche, K., 1992. Stage I and stage II propagation of short and long cracks in Al-Zn-Mg alloys, in: Short Fatigue Cracks. Presented at the ESIS 13, Mechanical Engineering Publications, London, pp. 135–151.

Radhakrishnan, V.M., 1980. Quantifying the parameters in fatigue crack propagation. Engineering Fracture Mechanics 13, 129–141. https://doi.org/10.1016/0013-7944(80)90048-X

Ritchie, R.O., Lankford, J., 1986. Small fatigue cracks: A statement of the problem and potential solutions. Materials Science and Engineering 84, 11–16. https://doi.org/10.1016/0025-5416(86)90217-X

Schijve, J., 1986. Fatigue crack closure, observations and technical significance (No. LR-485). Delft University of Technology.

Schijve, J., 1981. Shear lips on fatigue fractures in aluminium alloy sheet material. Engineering Fracture Mechanics 14, 789–800. https://doi.org/10.1016/0013-7944(81)90091-6

Stofanak, R.J., Hertzberg, R.W., Leupp, J., Jaccard, R., 1983. On the cyclic behavior of cast and extruded aluminum alloys. Part B: Fractography. Engineering Fracture Mechanics 17, 541–554.

Suresh, S., Ritchie, R.O., 1984. Propagation of short fatigue cracks. International Metals Reviews 29, 445–475. https://doi.org/10.1179/imtr.1984.29.1.445

Taylor, D., 1992. On the use of P-a plots to model the behaviour of short fatigue cracks. International Journal of Fatigue 14, 163–168. https://doi.org/10.1016/0142-1123(92)90369-N

Toribio, J., Álvarez, N., González, B., Matos, J.C., 2009. A critical review of stress intensity factor solutions for surface cracks in round bars subjected to tension loading. Engineering Failure Analysis 16, 794–809. https://doi.org/10.1016/j.engfailanal.2008.06.023

van der Walde, K., Hillberry, B.M., 2007. Initiation and shape development of corrosion-nucleated fatigue cracking. International Journal of Fatigue 29, 1269–1281. https://doi.org/10.1016/j.ijfatigue.2006.10.010

Wanhill, R.J.H., 1988. Low stress intensity fatigue crack growth in 2024-T3 and T351. Engineering Fracture Mechanics 30, 233–260. https://doi.org/10.1016/0013-7944(88)90227-5

Wilhem, D.P., 1967. Investigation of cyclic crack growth transitional behavior, in: Fatigue Crack Propagation, ASTM 415. ASTM Int., pp. 363–380.

Yoder, G.R., Cooley, L.A., Crooker, T.W., 1982. On microstructural control of near-threshold fatigue crack growth in 7000-series aluminum alloys. Scripta Metallurgica 16, 1021–1025. https://doi.org/10.1016/0036-9748(82)90448-3

Yoshinaka, F., Nakamura, T., Takeuchi, A., Uesugi, M., Uesugi, K., 2019. Initiation and growth behaviour of small internal fatigue cracks in Ti-6Al-4V via synchrotron radiation microcomputed tomography. Fatigue Fract Eng Mater Struct 42, 2093–2105. https://doi.org/10.1111/ffe.13085